P Selected for a Viewpoint in *Physics*

P H Y S I C A L   R E V I E W   L E T T E R S

# Multi-GeV Electron Beams from Capillary-Discharge-Guided Subpetawatt Laser Pulses in the Self-Trapping Regime

W. P. Leemans,[1,2,*] A. J. Gonsalves,[1] H.-S. Mao,[1] K. Nakamura,[1] C. Benedetti,[1] C. B. Schroeder,[1] Cs. Tóth,[1] J. Daniels,[1] D. E. Mittelberger,[2,1] S. S. Bulanov,[2,1] J.-L. Vay,[1] C. G. R. Geddes,[1] and E. Esarey[1]

[1]*Lawrence Berkeley National Laboratory, Berkeley, California 94720, USA*
[2]*Department of Physics, University of California, Berkeley, California 94720, USA*

Multi-GeV electron beams with energy up to 4.2 GeV, 6% rms energy spread, 6 pC charge, and 0.3 mrad rms divergence have been produced from a 9-cm-long capillary discharge waveguide with a plasma density of $\approx 7 \times 10^{17}$ cm$^{-3}$, powered by laser pulses with peak power up to 0.3 PW. Preformed plasma waveguides allow the use of lower laser power compared to unguided plasma structures to achieve the same electron beam energy. A detailed comparison between experiment and simulation indicates the sensitivity in this regime of the guiding and acceleration in the plasma structure to input intensity, density, and near-field laser mode profile.

Laser plasma accelerators (LPAs) can produce acceleration gradients on the order of tens to hundreds of GV/m, making them attractive as compact particle accelerators [1,2]. Over the past decade, significant progress has been made on LPAs, yielding quasimonoenergetic electron beams [3–5]. Previous experiments using preformed plasma channels from capillary discharge waveguides have demonstrated an acceleration of electron beams up to 1 GeV with 40 TW peak power laser pulses [6]. Subsequent experiments demonstrated > 1 GeV electron beams from nonpreformed plasmas using 200 TW laser pulses [7]. Recently, with the availability of petawatt class lasers, electron beams were produced in nonpreformed plasmas with energy up to 2 GeV using a 7-cm-long gas cell [8], and, using a dual gas jet system of 1.4 cm, beams with energy tails up to 3 GeV were observed [9]. GeV energy electron beams can be used for the generation of intense hard x rays and gamma rays [10,11]. For these and other applications, continued progress both in the maximum electron beam energy and in reducing the laser energy required to reach a given electron energy are important. In this Letter, experimental results and supporting numerical modeling are presented on the generation of electron beams with an energy of 4.2 GeV using 16 J of laser energy, significantly lower than previous experiments [8]. This was achieved by coupling laser pulses with high mode quality to preformed plasma channel waveguides produced by a 9-cm-long capillary discharge.

In these experiments, laser pulses at a wavelength $\lambda = 815$ nm $\pm 20$ nm were generated by the 1 Hz repetition rate Ti:sapphire-based BELLA laser [12] using a setup similar to what was used in Ref. [6], but with some key differences. The laser energy, $E_L$, delivered at the focal location was varied from tens of mJ to $\approx 16$ J. Typical pulse durations at optimum compression were $\tau_0 \simeq 40$ fs (FWHM) as measured by a frequency-resolved optical gating system. The

laser beam was imaged using two CCD cameras and an all-reflective achromatic telescope with two uncoated wedges to reduce the intensity (similar to Ref. [6]). The beam was imaged over a range of $\pm 20$ cm about the focus, and also at the plane of the first wedge 10.4 m downstream of focus. The first optical wedge and laser power meter each had a 23-mm-diam hole for the electron beam to pass through. The laser beam passing through these holes was reflected onto a beam dump using a 25-$\mu$m-thick gold coated foil, through which the electron beam passed.

The laser pulses were focused using a 13.5 m focal length off-axis parabolic mirror to a focal spot size of $w_0 \approx 52$ $\mu$m [Fig. 1(a)], where $w_0$ is defined as the radius at which the intensity drops to $1/e^2$ of the peak value. Measurement at 10.4 m downstream of focus showed the near field of the laser. The profile was close to a top hat [Fig. 1(b)], which is consistent with the ring profile observed 9 cm downstream of focus [Fig. 1(c)], and with measurements of the spot FWHM as a function of distance from focus. The hole in the wedge has only a minor impact for laser beams that are large in diameter compared to the hole size, as is the case here. The use of a deformable mirror and a wave-front sensor enabled high focal spot quality with a Strehl ratio of $0.8 \pm 0.1$. The associated normalized laser strength $a_0 = 8.5 \times 10^{-10} \lambda [\mu m] \sqrt{I_0 [\text{W/cm}^2]}$ where $I_0$ is the peak intensity and $a_0 = 1.6 \pm 0.1$ for 16 J input energy.

The electron beam profile at 11.1 m from the exit of the plasma structure was measured using a calibrated phosphor screen imaged onto a CCD camera. Charge was measured using two integrating current transformers, one located at 1 m from the exit of the plasma and one at 11.3 m. The beam energy was measured using a 2.5-m-long magnetic spectrometer (tunable up to 1.5 T and with a design similar to the spectrometer used in Ref. [6]) by imaging two
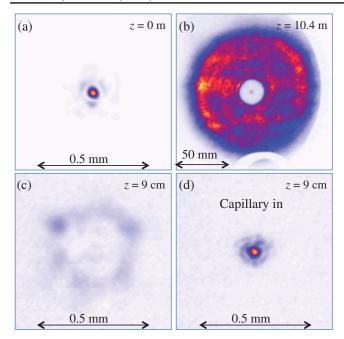
FIG. 1 (color). Typical laser spatial profiles in a vacuum with laser energy 16 J for (a) focus, (b) $z = 10.4$ m downstream of focus, and (c) $z = 9$ cm downstream of focus. The near field (b) shows an approximately top-hat profile. In (d) the guided mode is shown for plasma density $7.5 \times 10^{17}$ cm$^{-3}$. Well-confined high-quality modes were observed for densities as low as $2 \times 10^{17}$ cm$^{-3}$. The color scale is the same for (c) and (d).

phosphor screens of lengths 0.2 and 2.5 m at the exit plane of the spectrometer onto 12 CCD cameras.

The laser was guided by a preformed plasma channel, which provides several advantages for laser-plasma acceleration [3,6,13]. In such a channel, optimum guiding of a low-intensity transversely Gaussian laser pulse is obtained when the input laser mode size equals the matched spot size of the channel $w_0 = r_m$. Accessing higher LPA electron energies requires lower plasma density and longer plasmas [1]. Hence in the present experiments, the channel length was increased to 9 cm (from the 3.3 cm reported in Ref. [6]). Similarly, whereas previous experiments [6] used capillary discharge channels [14] with diameters ranging from 190–300 $\mu$m, here a 500-$\mu$m-diam channel was used due to the higher laser energy and spot size. The capillary discharge was operated with hydrogen using a current pulse of the form $I_{max} \exp(1 - e^{-z} - z)$, where $z = t/t_w$, $I_{max} = 250$ A and $t_w = 88$ ns. The laser pulses arrived $\approx 30$ ns after the peak of the current pulse. Channel formation occurred in the first $\approx 100$ ns of the current pulse and persisted for about 150 ns [15]. The on-axis densities employed were in the range of $0.2$–$1.5 \times 10^{18}$ cm$^{-3}$. The matched spot size of the channel was measured at low power levels to be $r_m \approx 60$ $\mu$m for the highest density of $1.5 \times 10^{18}$ cm$^{-3}$ and $r_m \approx 70$ $\mu$m for $n_e = 7 \times 10^{17}$ cm$^{-3}$, using laser centroid oscillations [16]. Figure 1(d) shows the mode at the exit of the 9-cm-long capillary with a plasma

density of $7.5 \times 10^{17}$ cm$^{-3}$ and a laser energy of 16 J, demonstrating the guiding of the laser pulse.

At the high intensities ($a_0 \gtrsim 1$) required for injection of electrons into the laser-excited plasma wave, the laser guiding properties can be strongly affected by relativistic effects and plasma wave excitation, and the matched guiding condition is laser-intensity dependent [17]. Simulations of laser propagation using the code INF&RNO [18] were conducted to evaluate the effects of both laser spatial mode and plasma (density and channel depth) on laser propagation in this experiment. The average measured laser pulse shape was used as input for the simulations, with an energy of 15 J in $\approx 40$ fs. The transverse profiles of the input laser pulses were modeled as both Gaussian—as is typically assumed for such simulations—and top-hat near-field profiles, which are more consistent with the data in Fig. 1. A top-hat near-field profile gives rise to a transverse intensity profile given by $I(r) \propto \{2[J_1(r/R)/(r/R)]\}^2$ at focus, where $J_1(x)$ is the first-order Bessel function of the first kind and $R$ is a scale parameter defining the width of the laser spot. The parameter $R$ was determined by measuring the FWHM of the laser intensity distribution at focus and using $R = \text{FWHM}/3.23$. Figure 2 shows the simulated laser pulse evolution as a
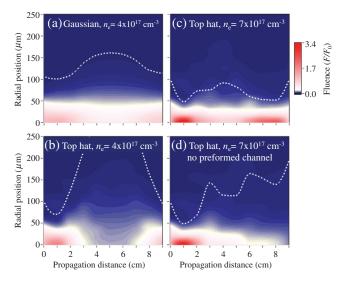


FIG. 2 (color). Laser pulse radial fluence profile evolution through the waveguide for different plasma density and initial fluence profiles for input laser energy 15 J. In each image the color scale represents the fluence (each normalized to the peak fluence at $z = 0$) and the dashed line is two times the radius at which the fluence drops to $1/e^2$ of the on-axis value. For (a) the initial laser pulse radial profile is Gaussian and the preformed channel is defined by $r_m = 93$ $\mu$m and $n_e = 4 \times 10^{17}$ cm$^{-3}$. In (b), (c), and (d) the near field of the laser pulse has a top-hat profile. For the same density and channel depth as in (a), (b) shows that the guiding is less efficient for the top-hat case. For (c) the combination of a self-guiding and a preformed plasma channel ($r_m = 81$ $\mu$m) mitigates diffraction over the full length of the plasma. Without a preformed plasma channel [panel (d)], self-guiding reduces the laser spot size for the first 2 cm but the laser diffracts strongly before the exit of the channel.

function of distance in the plasma. Figures 2(a) and 2(b) show that, although the mode at the output of a 500-$\mu$m-diam plasma waveguide after 9 cm of propagation in a preformed plasma channel density of $4 \times 10^{17}$ cm$^{-3}$ is similar for both top-hat and Gaussian beam profiles, the propagation in the channel for each profile is significantly different. The spot size in the middle of the capillary for the top-hat beam is larger for the same density, but plasma density increases can be used to control mode propagation. This is illustrated in Fig. 2(c), which shows a top-hat beam for a density of $7 \times 10^{17}$ cm$^{-3}$. Such a mitigation of diffraction can be important to avoid electron beam loss via phase slippage, resulting in the accelerating electrons entering defocusing wakefields (through the nonlinear decrease in plasma wavelength with decreasing intensity). In addition, guiding can minimize damage to the capillary walls caused by poor confinement of the laser beam. The simulations show that good guiding can be achieved in the high-intensity regime for both Gaussian and top-hat near-field profiles through a proper choice of plasma density. Without a preformed channel [see Fig. 2(d)], higher density results in an initial strong self-focusing of the laser beam, followed by strong diffraction.

Knowledge of the plasma density is essential for an understanding of guiding and electron acceleration. Since at high laser energies minor misalignment of the laser beam (at the 25 $\mu$m level) or operation at nonoptimum density can cause damage to the capillary structure (especially a narrowing of the gas feed slots that reduces the internal fill pressure), an *in situ* measurement is important. This is achieved by comparing experimental postinteraction laser spectra with simulations. As was shown in previous work [19], a high degree of accuracy can be obtained between experiments and simulations when using the measured laser pulse temporal and spatial profiles. Figure 3 shows the measured and simulated laser spectrum versus plasma density for an input laser energy of 7.5 J, corresponding to a peak power of $\approx$150 TW. The laser spectra obtained using the code INF&RNO were corrected for the instrument spectral response (with a diagnostic spectral range of
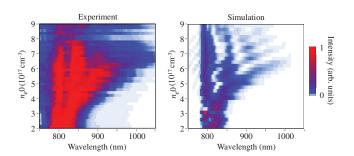
0.5–1.1 $\mu$m). The overall morphology of the measured and modeled output laser spectra matches well for a plasma density range of $2 \times 10^{17}$ cm$^{-3}$ to $9 \times 10^{17}$ cm$^{-3}$.

For sufficiently high intensities and an appropriate choice of density, plasma electrons were self-trapped and accelerated by the plasma wave. For a laser energy of 16 J and a pulse length of 40 fs (with a peak power of 300 TW), trapping in the 9-cm-long capillary was observed for a density $\gtrsim 3.4 \times 10^{17}$ cm$^{-3}$, producing beams of energy $\approx$1 GeV and a measurable charge above the detection threshold ($> 0.05$ pC). Electron beams above 3 GeV were observed for densities between $0.5 \times 10^{18}$ cm$^{-3}$ and $1 \times 10^{18}$ cm$^{-3}$, and for the higher end of that density range the beams had a charge of up to 180 pC with large energy spread. As electron beam generation relied on self-focusing and self-trapping, a high level of stability and reproducibility was not expected in comparison to methods that rely on triggered injection [20].

The angular fluctuation in electron beam pointing (which can be caused for example by pulse front tilt [21]) was larger than the $\approx$ 1 mrad acceptance of the spectrometer. Beams observed on the phosphor screen were not always observed on the magnetic spectrometer. For example, 30% of the shots showed a charge above 3 GeV, for a density range of $0.6$–$0.8 \times 10^{17}$ cm$^{-3}$. For the beams that were detected, the fluctuation on the high-energy peak was at the GeV level. Angular fluctuations can lead to both 0.5 GeV uncertainty in energy of observed electrons, and can cause parts of the beam to miss the entrance of the spectrometer.

The contribution of shot-to-shot fluctuations in experimental input parameters was investigated using particle-in-cell (PIC) simulations using the code INF&RNO for the range of the experimental fluctuations in plasma density and laser intensity. Fluctuations in the plasma density were estimated using measurements of group velocity delay [22] in a similar capillary that showed fluctuations of $\pm 0.2 \times 10^{17}$ cm$^{-3}$. The laser at the entrance of the plasma channel had rms fluctuation in $a_0$ of $\pm 0.08$, caused predominantly by temporal fluctuations. Table I summarizes the PIC simulations evaluating these experimental ranges. It shows that in addition to contributions from pointing errors, variation in observed electron beam energy can also result from variation in the laser intensity and plasma density.

The sensitivity to input parameter fluctuations can be understood by examining the laser propagation and the



FIG. 3 (color). Measured (left panel) and simulated (right panel) optical spectra at the output of the 500-$\mu$m-diam capillary as a function of plasma density for input laser energy $\approx$7.5 J and pulse duration $\approx$40 fs. The spectral response of the detection system was applied to the simulated data.

TABLE I. Results of PIC simulations using laser pulses with tophat nearfield profiles, illustrating the sensitivity of electron beam energy and charge to the input parameters.

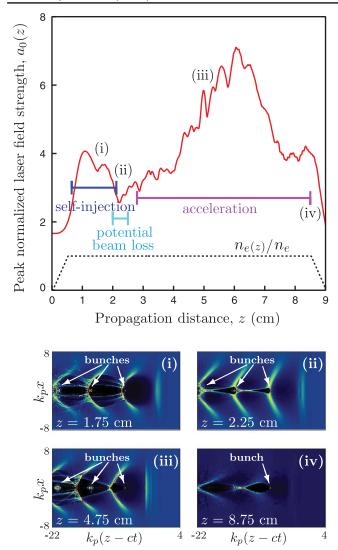| Density ($10^{17}$ cm$^{-3}$) | $E_L$ (J) | $a_0$ | Energy (GeV) | Charge (pC) |
|---|---|---|---|---|
| 6.5 | 16 | 1.66 | 3.9 | 15 |
| 7.0 | 16 | 1.66 | 4.3 | 50 |
| 7.0 | 15 | 1.61 | 3.7 | 35 |

FIG. 4 (color). Evolution (a) of the peak normalized laser field strength, $a_0(z)$ (red plot), in a PIC simulation for a top-hat laser pulse with an energy of 16 J focused at the entrance of a 9-cm-long plasma channel. The on-axis density (black dashed line) has a plateau density of $n_e = 7 \times 10^{17}$ cm$^{-3}$, and the matched radius is $r_m = 81$ $\mu$m. The wakefield (electron density) at various longitudinal locations is shown in (i)–(iv).

resulting acceleration physics observed in the simulations (Fig. 4). At the entrance of the plasma channel the laser-plasma interaction was in a quasilinear regime $a_0(z = 0) \simeq 1.66$. Self-focusing of the laser results in an increasing laser intensity, and the interaction enters the nonlinear bubble regime. After a propagation distance of $z \simeq 1$ cm, the normalized vector potential (the red curve in Fig. 4) reaches $a_0 \simeq 4.1$ and particle injection is observed in several wave periods behind the laser due to the large amplitude wake and a sufficiently low wake phase velocity [23]. Subsequently, the laser intensity decreases to a local minimum $a_0 \simeq 2.5$ for $z \simeq 2.2$ cm. Because of the intensity dependence of the nonlinear plasma wavelength [1], the period of the wake decreases, as shown in Fig. 4(ii).
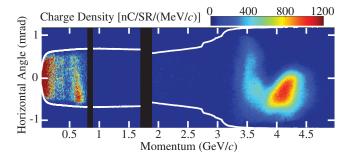


FIG. 5 (color). Energy spectrum of a 4.2 GeV electron beam measured using the broadband magnetic spectrometer. The plasma conditions closely match those in Fig. 2(c). The white lines show the angular acceptance of the spectrometer. The two black vertical stripes are areas not covered by the phosphor screen.

However, for this density, the plasma wavelength change is not enough to dephase the electrons, which continue to accelerate. For $z \gtrsim 2.5$ cm [Fig. 4(iii)] bunches are accelerated in the wakefield generated by the laser. The increase in peak normalized laser field strength observed for $2.5 < z < 6$ cm is due to laser self-steepening. For $z \gtrsim 6$ cm, the pulse length begins to increase due to laser redshifting, and the pulse starts losing resonance with the plasma. In this simulation, during the exit density ramp [Fig. 4(iv)] the self-injected bunches behind the first plasma period are lost due to the defocusing wakefield generated by the bunch in the first plasma period and the residual laser wakefield, yielding a single electron beam emerging from the plasma.

The value of the minimum of $a_0$ in region (ii) of Fig. 4, and therefore the electron bunch phasing, depends sensitively on the details of the laser-plasma parameters. For instance, in a simulation with a lower on-axis density, namely, $n_e = 6.2 \times 10^{17}$ cm$^{-3}$, where the normalized laser field strength reaches the minimum value $a_0 \simeq 2$, the reduction of the plasma wavelength moves the self-injected bunches out of the focusing and accelerating phase of the wake, leading to complete electron beam loss. This indicates that, due to different laser propagation, modest changes to the laser intensity or plasma density can cause large modifications of the final electron beam properties.

One of the lowest energy spread high-energy beams (shown in Fig. 5) was obtained for a plasma density of $7 \times 10^{17}$ cm$^{-3}$ and 16 J laser energy. The electron beam energy was $4.2^{+0.6}_{-0.4}$ GeV with 6% spread (rms), a measured charge of $6 \pm 1$ pC, and a divergence of 0.3 mrad (rms). The uncertainty in the electron beam energy was due to the angular acceptance of the spectrometer.

In conclusion, the experiments demonstrate that laser pulses with peak power at the few hundred terawatt level propagating in preformed channels can generate multi-GeV electron beams. Preformed plasma channels used with high Strehl ratio laser pulses allowed high-energy (4.2 GeV) beams to be produced with laser energy (16 J) significantly less than that used to produce 2 GeV beams [8]. Through experiments and simulations, it is found that the

non-Gaussian nature of the near-field laser beam profile requires operation at higher density than for a Gaussian beam to ensure good guiding. This has important consequences for the maximum energy that can be reached and will require the implementation of techniques such as laser heating [24] to deepen the radial plasma profile and thereby enhance confinement and lower the on-axis density. Provided that the slice energy spread and the emittance are sufficiently low, electron beams with the achieved energy could power x-ray free-electron lasers [25]. Future experiments will employ techniques to both provide better guiding of the laser pulse and triggered injection [20] for acceleration at lower densities (with longer dephasing and pump depletion lengths) and improve reproducibility. Simulations indicate that this will allow for the generation of electron beam energies at the 10 GeV level using 40-J, 100-fs laser pulses [26].

*WPLeemans@lbl.gov

[1] E. Esarey, C. B. Schroeder, and W. P. Leemans, Rev. Mod. Phys. **81**, 1229 (2009).
[2] S. M. Hooker, Nat. Photonics **7**, 775 (2013).
[3] C. G. R. Geddes, Cs. Tóth, J. van Tilborg, E. Esarey, C. B. Schroeder, D. Bruhwiler, C. Nieter, J. Cary, and W. P. Leemans, Nature (London) **431**, 538 (2004).
[4] J. Faure, Y. Glinec, A. Pukhov, S. Kiselev, S. Gordienko, E. Lefebvre, J.-P. Rousseau, F. Burgy, and V. Malka, Nature (London) **431**, 541 (2004).
[5] S. P. D. Mangles, C. D. Murphy, Z. Najmudin, A. G. R. Thomas, J. L. Collier, A. E. Dangor, E. J. Divall, P. S. Foster, J. G. Gallacher, C. J. Hooker, D. A. Jaroszynski, A. J. Langley, W. B. Mori, P. A. Norreys, F. S. Tsung, R. Viskup, B. R. Walton, and K. Krushelnick, Nature (London) **431**, 535 (2004).
[6] W. P. Leemans, B. Nagler, A. J. Gonsalves, Cs. Tóth, K. Nakamura, C. G. R. Geddes, E. Esarey, C. B. Schroeder, and S. M. Hooker, Nat. Phys. **2**, 696 (2006).
[7] C. E. Clayton, J. E. Ralph, F. Albert, R. A. Fonseca, S. H. Glenzer, C. Joshi, W. Lu, K. A. Marsh, S. F. Martins, W. B. Mori, A. Pak, F. S. Tsung, B. B. Pollock, J. S. Ross, L. O. Silva, and D. H. Froula, Phys. Rev. Lett. **105**, 105003 (2010).
[8] X. Wang et al., Nat. Commun. **4**, 1988 (2013).
[9] H. T. Kim, K. H. Pae, H. J. Cha, I. J. Kim, T. J. Yu, J. H. Sung, S. K. Lee, T. M. Jeong, and J. Lee, Phys. Rev. Lett. **111**, 165002 (2013).
[10] S. Kneip et al., Nat. Phys. **6**, 980 (2010).
[11] S. Cipiccia et al., Nat. Phys. **7**, 867 (2011).
[12] W. P. Leemans, J. Daniels, A. Deshmukh, A. J. Gonsalves, A. Magana, H. S. Mao, D. E. Mittelberger, K. Nakamura, J. R. Riley, D. Syversrud, Cs. Tóth, and N. Ybarrolaza, in Proceedings of PAC2013, Pasadena, CA, 2013 (JACoW, Geneva, 2013), p. 1097.
[13] T. P. A. Ibbotson et al., Phys. Rev. ST Accel. Beams **13**, 031301 (2010).
[14] A. Butler, D. J. Spence, and S. M. Hooker, Phys. Rev. Lett. **89**, 185003 (2002); A. J. Gonsalves, T. P. Rowlands-Rees, B. H. P. Broks, J. J. A. M. van der Mullen, and S. M. Hooker ibid. **98**, 025002 (2007).
[15] N. A. Bobrova, A. A. Esaulov, J. I. Sakai, P. V. Sasorov, D. J. Spence, A. Butler, S. M. Hooker, and S. V. Bulanov, Phys. Rev. E **65**, 016407 (2001).
[16] A. J. Gonsalves, K. Nakamura, C. Lin, J. Osterhoff, S. Shiraishi, C. B. Schroeder, C. G. R. Geddes, Cs. Tóth, E. Esarey, and W. P. Leemans, Phys. Plasmas **17**, 056706 (2010).
[17] C. Benedetti, C. B. Schroeder, E. Esarey, and W. P. Leemans, Phys. Plasmas **19**, 053101 (2012).
[18] C. Benedetti, C. B. Schroeder, E. Esarey, and W. P. Leemans, in Proceedings of ICAP2012, Rostock-Warnemünde, Germany, 2012 (JACoW, Geneva, 2012), p. THAAI2.
[19] S. Shiraishi, C. Benedetti, A. Gonsalves, K. Nakamura, B. Shaw, T. Sokollik, J. van Tilborg, C. Geddes, C. B. Schroeder, Cs. Tóth, E. Esarey, and W. Leemans, Phys. Plasmas **20**, 063103 (2013).
[20] A. J. Gonsalves, K. Nakamura, C. Lin, D. Panasenko, S. Shiraishi, T. Sokollik, C. Benedetti, C. B. Schroeder, C. G. R. Geddes, J. van Tilborg, J. Osterhoff, E. Esarey, Cs. Tóth, and W. P. Leemans, Nat. Phys. **7**, 862 (2011).
[21] A. Popp, J. Vieira, J. Osterhoff, Z. Major, R. Hörlein, M. Fuchs, R. Weingartner, T. P. Rowlands-Rees, M. Marti, R. A. Fonseca, S. F. Martins, L. O. Silva, S. M. Hooker, F. Krausz, F. Grüner, and S. Karsch, Phys. Rev. Lett. **105**, 215001 (2010).
[22] J. van Tilborg, J. Daniels, A. J. Gonsalves, C. B. Schroeder, E. Esarey, and W. P. Leemans, Phys. Rev. E **89**, 063103 (2014).
[23] C. Benedetti, C. B. Schroeder, E. Esarey, F. Rossi, and W. P. Leemans, Phys. Plasmas **20**, 103108 (2013).
[24] N. A. Bobrova, P. V. Sasorov, C. Benedetti, S. S. Bulanov, C. G. R. Geddes, C. B. Schroeder, E. Esarey, and W. P. Leemans, Phys. Plasmas **20**, 020703 (2013).
[25] A. R. Maier, A. Meseck, S. Reiche, C. B. Schroeder, T. Seggebrock, and F. Grüner, Phys. Rev. X **2**, 031019 (2012); Z. Huang, Y. Ding, and C. B. Schroeder, Phys. Rev. Lett. **109**, 204801 (2012).
[26] W. P. Leemans, R. Duarte, E. Esarey, S. Fournier, C. G. R. Geddes, D. Lockhart, C. B. Schroeder, Cs. Tóth, J.-L. Vay, and S. Zimmermann, AIP Conf. Proc. **1299**, 311 (2010).